PCCP

# Dielectric Characteristics of Fast Li ion Conducting Garnet-Type Li5+2xLa3Nb2-xYxO12 (x = 0.25, 0.5 and 0.75)



| | |
|---|---|
| Journal: | *Physical Chemistry Chemical Physics* |
| Manuscript ID | CP-ART-04-2016-002287.R1 |
| Article Type: | Paper |
| Date Submitted by the Author: | 02-May-2016 |
| Complete List of Authors: | Narayanan, Sumaletha; University of Calgary, Chemistry<br>Baral, Ashok; University of Calgary, Department of Chemistry<br>Thangadurai, Venkataraman; University of Calgary, Department of Chemistry |
| | |

# Dielectric Characteristics of Fast Li ion Conducting Garnet-Type $Li_{5+2x}La_3Nb_{2-x}Y_xO_{12}$ (x = 0.25, 0.5 and 0.75)

Sumaletha Narayanan, Ashok Kumar Baral, and Venkataraman Thangadurai*

Department of Chemistry, University of Calgary, 2500 University Dr NW, Calgary, AB, T2N1N4, Canada, For correspondence: vthangad@ucalgary.ca; phone: 1403 210 8649

**ABSTRACT.** Here, we report the dielectric characteristics of Li-stuffed garnet-type $Li_{5+2x}La_3Nb_{2-x}Y_xO_{12}$ (x = 0.25, 0.5 and 0.75) in the temperature range of about -53 to 50 °C using ac impedance spectroscopy. All the investigated Li-stuffed garnet compounds were prepared, under the same condition, using conventional solid state reaction at elevated temperature in air. The Nyquist plots show manily bulk contribution to the total $Li^+$ ion conductivity for $Li_{5.5}La_3Nb_{1.75}Y_{0.25}O_{12}$ ($Li_{5.5}$-Nb) and $Li_6La_3Nb_{1.5}Y_{0.5}O_{12}$ ($Li_6$-Nb), while both bulk and grain-boundary effects are visible in case of $Li_{6.5}La_3Nb_{1.25}Y_{0.75}O_{12}$ ($Li_{6.5}$-Nb) phase at ~ -22 °C. Non-Debye relaxation process was observed in the modulus ac impedance plots. The tangent loss of $Li_{5+2x}La_3Nb_{2-x}Y_xO_{12}$ are compared with that of corresponding Ta analogue, $Li_{5+2x}La_3Ta_{2-x}Y_xO_{12}$ and showed a decrease in peak intensity in the Nb-based garnet samples attribute to slight increase in its $Li^+$ ion conductivity. The relative dielectric constant values also found to be higher for Ta member (> 60 for $Li_{5+2x}La_3Ta_{2-x}Y_xO_{12}$) than that of the corresponding Nb analogue (~50 for $Li_{5+2x}La_3Nb_{2-x}Y_xO_{12}$) at below room temperature. A long-range order $Li^+$ ion migration pathway with relaxation time ($\tau_0$) $10^{-18}$ - $10^{-15}$ s and an activation energy of 0.59 - 0.40 eV was observed for the investigated $Li_{5+2x}La_3Nb_{2-x}Y_xO_{12}$ garnets and is comparable to that of the corresponding Ta-based $Li_{5+2x}La_3Ta_{2-x}Y_xO_{12}$ garnets.

## INTRODUCTION

Currently, lithium ion batteries (LIBs) attain much attention because of their high volumetric and gravimetric energy densities, which make them suitable for possible applications from portable devices to electric vehicles and grid scale to support the peak power demand. However, there is a long-term remaining safety concern related to the presently used organic polymer-based $Li^+$ ion electrolytes in LIBs and they must be replaced with thermally stable fast $Li^+$ ion conductors. To this end, several families of inorganic metal oxides and non-oxides have been investigated, of which recently discovered, Li-stuffed garnets-type metal oxides are potential class of solid-state $Li^+$ ion conductors for all-solid-state LIBs due to their excellent physical and chemical properties.[1-7] Briefly, the garnet structure is known to accommodate of Li contents ranging from 24 to 56 ions per unit cell. Increasing Li content in Li-stuffed garnet decreases the occupation of tetrahedral $Li^+$ ions and increases the population of octahedral coordinated $Li^+$ ions in the crystal structure.[8] Except $Li_3$-phase, $Li_3Ln_3Te_2O_{12}$ (Ln = Y, Pr, Nd, Sm-Lu), the $Li^+$ ions in tetrahedral and octahedral sites are partially filled in all other known Li-stuffed garnets, which make them unique structural disorders for fast ion conduction.[9] Doping $Ba^{2+}$ for $La^{3+}$ and $Zr^{4+}$ for $Nb^{5+}/Ta^{5+}$ showed increase in the conductivity of the parent $Li_5La_3M_2O_{12}$ (M = Nb, Ta).[10, 11] To date, garnet with the nominal chemical formula $Li_{6.4}La_3Zr_{1.4}Ta_{0.6}O_{12}$, exhibits the highest bulk $Li^+$ ion conductivity of $10^{-3}$ $Scm^{-1}$ at room temperature with an activation energy 0.35 eV (25-157 °C).[12] Zr and Ta-based garnets were found to be chemically stable to Li anodes and showed electrochemical stability window up to 6 V/Li.[13, 14] The highly dense crystal structure makes it harder to understand the role of chemical doping at Li, La and M or M/ sites in Li-stuffed $Li_5La_3M_2O_{12}$, $Li_6La_2AM_2O_{12}$ (M = Ta, Nb; A = Ca, Sr, Ba), and $Li_7La_3M'_2O_{12}$ (M/ = Zr, Sn) garnets of $Li^+$ ion transport properties.[15, 16] Creating

oxide ion vacancies by aliovalent doping at Nb-sites in $Li_5La_3Nb_2O_{12}$ decreases the bulk $Li^+$ ion conductivity.[17]

It is important to understand the $Li^+$ ion conduction mechanism in garnets to further improve $Li^+$ ion conduction for advanced all-solid-state Li ion battery. It was predicted that the $Li^+$ ions at octahedral sites in the garnet structure, are mainly attribute to the fast ionic conduction and and tetrahedral sites $Li^+$ ions seem to be responsible for maintaining the stability of the garnet framework structure.[8] Solid State $^7$Li MAS NMR and density functional theory (DFT) studies further support above proposed $Li^+$ ion conduction mechanism in the garnet structure.[18, 19] So far, several studies have been carried out to understand the $Li^+$ ion dynamics in these Li-stuffed garnets using solid state techniques such as neutron diffraction, nuclear magnetic resonance, electrochemical ac impedance spectroscopy and DFT calculations.[8, 10, 19-31] The present study is focused to analyze the dielectric properties of $Li_{5+2x}La_3Nb_{2-x}Y_xO_{12}$ (x = 0.25, 0.5 and 0.75) using electrochemical ac impedance spectroscopy to better understand the $Li^+$ ion conduction mechanism in the Li-stuffed garnets.

## EXPERIMENTAL

Single phase cubic structure garnet-type $Li_{5+2x}La_3Nb_{2-x}Y_xO_{12}$ (x = 0.25, 0.5 and 0.75 which are represented as $Li_{5.5}$-Nb, $Li_6$-Nb and $Li_{6.5}$-Nb, respectively) were prepared by solid state reaction at elevated temperature.[32] The stoichiometric amount of the precursors of high purity $LiNO_3$ (99%, Alfa Aesar), $La_2O_3$ (99.99%, Alfa Aesar, preheated at 900 °C for 24 h), $Nb_2O_5$ (99.5%, Alfa Aesar), and $Y(NO_3)_3$ (99.9%, Alfa Aesar) were ball milled to ensure homogeneity. 10 wt. % excess $LiNO_3$ was added to compensate the loss of lithium oxide while sintering. Heating at different stages were carried out at 700 °C/6 h, 900 °C/24 h and 1100 °C/6 h. The dielectric analyses were carried out using the ac impedance spectroscopy employing a Solartron 1260

impedance/gain-phase analyzer (0.01 Hz to 1 MHz) in the temperature range of -53 to 50 °C in air. Temperature was controlled in below room temperature using dry ice.[33] The pellet garnet samples for ac impedance measurements were painted with Au paste on both sides and were cured for 1 h at 600 °C.

## RESULTS AND DISCUSSION

### AC Impedance Spectroscopy

Typical AC impedance spectra of cubic structured garnet-type $Li_{5+2x}La_3Nb_{2-x}Y_xO_{12}$[32] (x = 0.25, 0.5 and 0.75 which are represented as $Li_{5.5}$-Nb, $Li_6$-Nb and $Li_{6.5}$-Nb, respectively) at -22 °C are shown in Figure 1. The $Li_{5.5}$-Nb and $Li_6$-Nb phases of $Li_{5+2x}La_3Nb_{2-x}Y_xO_{12}$ show a single semicircle at about -53 to 50 °C, which correspond to bulk (b) contribution at higher frequency range and a spike at the low-frequency range due to polarization resistance. The line spacing through the data point is fitted using an equivalent circuit consisting of $(R_bCPE_b)(CPE_e)$ for $Li_{5.5}$-Nb and $Li_6$-Nb (where $R_b$ is the bulk resistance, $CPE_b$ is the constant phase element due to bulk and $CPE_e$ is the constant phase element due to electrode). The $R_b$ is low-frequency intercerpt to real axis and bulk capacitance was found to be in the order of ~ $10^{-11}$ F. The $Li_{6.5}$-Nb phase shows an additional distorted semi-circle corresponding to grain-boundary (gb) contribution (capacitance ~ $10^{-8}$ F) at low-frequency and it can be described using an equivalent circuit $(R_bCPE_b)(R_{gb}\ CPE_{gb})\ (CPE_e)$ (where $R_{gb}$ is the gb resistance, $CPE_{gb}$ is the constant phase element due to gb). The electrode capacitane was found to be in the order of $10^{-7}$ F. As reported earlier,[32] the density of the $Li_{5+2x}La_3Nb_{2-x}Y_xO_{12}$ garnet was found to be increasing with increase in Y and Li content. Also, there are some impurity peaks observed in PXRD of highly doped $Li_{6.5}La_3Nb_{1.25}Y_{0.75}O_{12}$ ($Li_{6.5}$-Nb) phase. These factors might be contributing to the presence of grain-boundary arc visible in $Li_{6.5}$-Nb compared to $Li_{5.5}La_3Nb_{1.75}Y_{0.25}O_{12}$ ($Li_{5.5}$-Nb) and $Li_6La_3Nb_{1.5}Y_{0.5}O_{12}$ ($Li_6$-Nb). The total resistance (*R*) (bulk +grain-boundary) was used to

estimate the total $Li^+$ ion conductivity ($\sigma$) from the low-frequency intercept point of $Z''$ (imaginary part of impedance) to the X-axis ($Z'$, real part of the impedance) (Figure 1). The $Li^+$ ion conductivity was calculated using the equation 1:

$$\sigma = \left(\frac{1}{R}\right)\left(\frac{l}{a}\right) \quad (1)$$

where $l$ is the sample thickness and $a$ is the area of current collector. The $Li^+$ ion conductivity dependence on temperature was represented by the Arrhenius plots (Figure 2) and they can be described using the equation 2:

$$\sigma T = A\exp^{\left(-\frac{E_a}{kT}\right)} \quad (2)$$

where $T$ is the temperature, $A$ is the pre-exponential factor, $E_a$ is the activation energy, and $k$ is the Boltzmann's constant ($1.38 \times 10^{-23}$ $JK^{-1}$). The $Li^+$ ion conductivity of samples increases from ($Li_{5.5}La_3Nb_{1.75}Y_{0.25}O_{12}$ ($Li_{5.5}$-Nb) to $Li_{6.5}La_3Nb_{1.25}Y_{0.75}O_{12}$ ($Li_{6.5}$-Nb) which is consistent with the increase in cell parameter ($a$) calculated from powder X-ray diffraction (PXRD). The cell constant was found to be 12.8582(5) Å, 12.9136(4) Å and 12.9488(11) Å) for ($Li_{5.5}La_3Nb_{1.75}Y_{0.25}O_{12}$ ($Li_{5.5}$-Nb), $Li_6La_3Nb_{1.5}Y_{0.5}O_{12}$ ($Li_6$-Nb), and $Li_{6.5}La_3Nb_{1.25}Y_{0.75}O_{12}$ ($Li_{6.5}$-Nb), respectively.[32] The activation energy calculated for $Li_{5.5}$-Nb, $Li_6$-Nb and $Li_{6.5}$-Nb phases are 0.59, 0.58 and 0.42 eV, respectively, in the temperature range of -53 to 50 °C (Table 1) which is in agreement with the $Li^+$ ion conductivity trend.

The relationship of conductivity (σ) and frequency is expressed by Jonscher universal power law [34] i.e.,: $\sigma_\omega = \sigma_{dc} + A\omega^n$ (3)

where $\omega$ is the angular frequency, $\sigma_{dc}$ is the dc conductivity, $A$ is the proportionality constant, and $n$ is the power factor which varies from 0 to 1. Shown in Figure 3 is the $Li^+$ ion conductivity as a function of frequency for $Li_{5+2x}La_3Nb_{2-x}Y_xO_{12}$ in the temperature range at -53 to 50 °C. The dispersion region seen at lower frequency range is due to the polarization due to $Li^+$ ion-blocking electrode. The frequency independent dc plateau region is seen at lower frequency range followed by a dispersion region. This could be explained by jump relaxation model which indicates that at low frequencies, the ions hop from one site to the neighboring vacancy site contribute to the dc conductivity, and at higher frequencies the correlated alternative hopping along with relaxation of ions contribute to the conductivity relaxation at the dispersion region.[35, 36] For garnet-type oxide, the jumping of $Li^+$ ions from one octahedral site to other octahedral-site (for e.g., 48g-site to the 96h-site) followed by the readjustment of surrounding ions causes the conductivity relaxation.[25]

The real ($\varepsilon'$) and imaginary ($\varepsilon''$) part of permittivity ($\varepsilon$) can was computed using the equations 4 and 5 as shown below:[37]

$$\varepsilon' = -\frac{Z''}{\omega C_0 (Z'^2 + Z''^2)} \quad (4)$$

$$\varepsilon'' = -\frac{Z'}{\omega C_0 (Z'^2 + Z''^2)} \quad (5)$$

where $C_o$ is the vacuum capacitance of the cell which is represented as $C_o = \varepsilon_{o(A/d)}$ (where $\varepsilon_o$ is the permittivity of free space = 8.854 x $10^{-14}$ $Fcm^{-1}$, $A$ is the electrode area and $d$ is the thickness of the sample). Figure 4 shows the relation between the real part of permittivity ($\varepsilon'$) and frequency at different temperatures. It is noticeable that the dielectric constant decreases

exponentially with frequency showing a constant minimum value. The upturn at the lower frequency region may be due to the blocking electrode-electrolyte polarization at the interface. When the frequency is increased, the periodical reversal of the field is increased and as a result the oscillating charges contribute to the dielectric constant. This causes a decrease in dielectric constant with increase in frequency. Dipolar polarization leads to formation of plateau at the low-frequency region at higher temperature, which is clearly visible in the case of $Li_{6.5}$-Nb phase and also in the Ta series, $Li_{5+2x}La_3Ta_{2-x}Y_xO_{12}$ (x = 0.25, 0.5 and 0.75).[25] Shifting of plateau towards high frequencies with increasing temperature indicate the increase in frequency of dipolar rotations, as $Li^+$ ion mobility is enhanced due to the thermal activation.[38]

The plot of imaginary part of the dielectric permittivity ($\varepsilon''$) against frequency is illustrated in Figure 5a, b and c. $\varepsilon''$ is the dielectric loss factor which is the combination of dipolar loss and conduction loss. The conduction loss is predominant at lower temperatures and appears as a straight line and shows inverse relationship to the angular frequency ($\omega$) especially for $Li_{5.5}$-Nb and $Li_6$-Nb phases (Figure 5a and b). In all the cases, the peak/plateau at lower frequencies due to dipolar polarization was observed (Figure 4).

The dielectric tangent loss as a function of frequency of $Li_{5+2x}La_3Nb_{2-x}Y_xO_{12}$ is shown in Figure 6. The peak observed in $Li_{5.5}$-Nb and $Li_6$-Nb phases can be attributed to the loss due to Li-Li-dipolar interaction under the applied electrical field.[25] There seem two relaxation peaks for $Li_{6.5}$-Nb phases at intermediate frequencies, suggesting that an additional polarization loss occurs when compared to the $Li_{5.5}$-Nb and $Li_6$-Nb phases. The higher frequency peak may be attributed to the loss due to Li-Li dipolar rotation in the bulk ionic conductivity.[39] The lower frequency peak in Figure 6c may be due to the dielectric loss, as a result of grain-boundary polarization. This is consistent with the appearance of grain-boundary arc in the AC impedance spectrum of

$Li_{6.5}$-Nb phase (Figure 1). The shift in tangent loss peaks towards higher frequencies with increase in temperature, simiar to real part of permittivity ($\varepsilon'$) as a funcation of temperature, indicates that both grain-boundary space charge polarization and Li-Li dipolar interaction in bulk are thermal activated processes.

In Figure 7, the tangent loss of both Nb with Ta members of $Li_{5+2x}La_3M_{2-x}Y_xO_{12}$ (M = Nb, Ta) at different temperatures is compared. A similar plot is observed, except for $Li_{6.5}$-Nb phase of Nb series $Li_{5+2x}La_3Nb_{2-x}Y_xO_{12}$, correspond to bulk and grain-boundary contribution.[32] However, very small values of peak intensity of $Li_{5+2x}La_3Nb_{2-x}Y_xO_{12}$ (Figures 7b and 7c) compared to that of Ta series $Li_{5+2x}La_3Ta_{2-x}Y_xO_{12}$ indicated that either there are lesser number of dipoles in Nb garnets than Ta garnets or the mobility of ions is higher in the presently investigated Nb garnets leading to a quick response of Li-Li dipoles to external electric field and resulting in a less dielectric loss. Overall, the dielectric relaxation can be considered due to the main-body interactions as is common for the ionic conductor.[34] The relative permittivity/dielectric constant ($\varepsilon_r$) of $Li_{5+2x}La_3M_{2-x}Y_xO_{12}$ (M = Nb, Ta[32]) were calculated using the capacitance (C), as given in equation 6 and the results are summarized in Figure 8.

$$C = \varepsilon_o \varepsilon_r \frac{A}{d} \qquad (6)$$

Dielectric constant slightly increases with increase in Li content in Ta series materials, although there is no trend in variation of $\varepsilon_r$ with Li content in Nb series. With increase in temperature, value of dielectric constant is increased in both Nb and Ta based garnets. The dielectric constant of Nb garnets is found to be relatively higher than that of Ta garnets. Higher is the dielectric constant; generally, greater is the polarizability of medium. Thus, higher dielectric constant (Figure 8) and lower dielectric loss (Figure 7) in Nb series materials indicate that its $Li^+$ ion

mobility seems to be higher compared to that of Ta garnets since both Nb and Ta oxides exhibit similar ionic radius and electronic structure. A comparison of $Li^+$ ionic conductivity of both Nb and Ta phases of $Li_{5+2x}La_3M_{2-x}Y_xO_{12}$ at specific temperatures is shown in Table 2.[7, 25, 32]

Using modulus analysis, it is possible to understand the bulk relaxation properties in more details by suppressing the lower frequency phenomena, especially the electrode effect.[30] The complex dielectric modulus is expressed as equation 7:

$$M = j\omega C_o(Z^{/} + Z^{//}) \qquad (7)$$

where the real and imaginary parts can be separated as $M^{/} = \omega C_o Z^{/}$ and $M^{//} = -\omega C_o Z^{//}$. The electric modulus accounts for the electric field relaxation in the material at a constant electric displacement.[40] The modulus spectra of $Li_{5.5}$-Nb, $Li_6$-Nb and $Li_{6.5}$-Nb phases of $Li_{5+2x}La_3Nb_{2-x}Y_xO_{12}$ samples, measured at a temperature range of -53 to -21 ºC as a function of frequency is shown in Figure 9. The electric modulus ($M^{//}$) shows a frequency independent behavior at the lower frequency region for all the samples. This indicates that the electrode polarization does not contribute to the electric modulus and the long-range migration of $Li^+$ ion by hopping from one site to the neighboring site.[30] Presence of peak in the modulus spectra means the relaxation associated with $Li^+$ ion mobility.[25, 30] The appearance of high frequency side peak at lower temperatures could be due to the $Li^+$ ion re-orientation relaxation as $Li^+$ ion moves from one octahedron to another octahedron around the immobile tetrahedral site.[25] The shift in peak position towards higher frequency side with increase in temperature indicates that $Li^+$ ion relaxation re-orientation is thermally activated phenomenon. Also, it is noticeable that the peak tend to disappear in $Li_{6.5}$-Nb phase which can be explained in terms of long-range order migration of $Li^+$ ion instead of local migration as seen in other members.[25]

The relaxation time, $\tau$ is related to the frequency maximum in the modulus plots, $f_M^{//}$ as shown in equation 8:

$$\tau = \frac{1}{2\pi f_{M^{//}}} \quad (8)$$

which can actually reveal the short range and or long range migration of $Li^+$ in the crystal structure. Figure 10 shows the Arrhenius behavior of relaxation time, τ for the local motion of $Li^+$ according to the equation 9:

$$\tau = \tau_0 \exp\left(\frac{-E_m}{k_B T}\right) \quad (9)$$

where $\tau_0$ is the relaxation time at infinite temperature, $E_m$ is the migration energy. The migration energy calculated for $Li_{5.5}$-Nb, and $Li_6$-Nb and $Li_{6.5}$-Nb phases are 0.59, and 0.52, and 0.40 eV, respectively which is close to the theoretically calculated activation energy. The relaxation time, $\tau_0$ calculated was in the range of $10^{-15}$ _ $10^{-18}$ s with a decrease in which is comparable with that of Ta family, $Li_{5+2x}La_3Ta_{2-x}Y_xO_{12}$.[25] The ac impedance or NMR analysis of some of the ionic conductors is mentioned here to get an idea of how the relaxation time is varied in different systems. In the polymer nano-composites of polyethylene oxide and lithium perchlorate, $Li^+$ ions show relaxation times in micro seconds ($10^{-6}$ s).[41] The fastest Na ion conducting, Na β-alumina, has exhibited a relaxation time, $\tau_0$ of $10^{-12}$ s.[42] Solid State $^7$Li NMR analysis of $Li_{1.3}Al_{0.15}Y_{0.15}Ti_{1.7}(PO_4)_3$ showed a relaxation time in the order of $10^{-12}$ s.[43] For $(BiI_3)_{0.4}$-$(Ag_3PO_4)_{0.6}$ electrolyte, the mobile $Ag^+$ ions show the relaxation time of $10^{-7}$ - $10^{-11}$ s.[44]

## CONCLUSIONS

The transport mechanism of $Li_{5+2x}La_3Nb_{2-x}Y_xO_{12}$ (x = 0.25, 0.5 and 0.75) was studied in terms of their dielectric behavior at below room temperature. The bulk $Li^+$ ion conductivity of samples increases with increase in Li content and follows the trend $Li_{5.5}La_3Nb_{1.75}Y_{0.25}O_{12}$ ($Li_{5.5}$ -Nb) < $Li_6La_3Nb_{1.5}Y_{0.5}O_{12}$ ($Li_6$-Nb) < $Li_{6.5}La_3Nb_{1.25}Y_{0.75}O_{12}$ ($Li_{6.5}$-Nb) and also follows with the cell contant trend. The $Li^+$ ion conductivity as a function of frequency was found to obey the Jonscher universal power law. The modulus plots indicate the non-Debye behavior of $Li^+$ ion relaxation. The decrease in relative dielectric constant for Nb members compared to that of Ta members of $Li_{5+2x}La_3Nb_{2-x}Y_xO_{12}$ (M = Nb, Ta) could be explained in terms of higher dipole moment and lesser $Li^+$ ion mobility. The relaxation time, $\tau_0$, calculated was $10^{-18}$, $10^{-17}$ and $10^{-15}$ s and activation energy observed was 0.59, 0.52 and 0.40 eV for $Li_{5.5}$-Nb, $Li_6$-Nb and $Li_{6.5}$-Nb, respectively, of $Li_{5+2x}La_3Nb_{2-x}Y_xO_{12}$ from the relaxation profile.

## ACKNOWLEDGEMENTS

The funding support from Natural Sciences and Engineering Research Council of Canada (NSERC) through Discovery Grants (DG) program is acknowledged for this work.

## REFERENCES

1. V. Thangadurai, S. Narayanan and D. Pinzaru, *Chem. Soc. Rev.*, 2014, **43**, 4714-4727.
2. V. Thangadurai, D. Pinzaru, S. Narayanan and A. K. Baral, *J. Phys. Chem. Lett.*, 2015, **6**, 292-299.
3. L. Cheng, W. Chen, M. Kunz, K. Persson, N. Tamura, G. Chen and M. Doeff, *ACS Appl. Mater. Interfaces*, 2015, **7**, 2073-2081.

4. A. Gupta, R. Murugan, M. P. Paranthaman, Z. Bi, C. A. Bridges, M. Nakanishi, A. P. Sokolov, K. S. Han, E. W. Hagaman, H. Xie, C. B. Mullins and J. B. Goodenough, *J. Power Sources*, 2012, **209**, 184-188.

5. Y. Li, C.-A. Wang, H. Xie, J. Cheng and J. B. Goodenough, *Electrochem. Commun.*, 2011, **13**, 1289-1292.

6. S. Narayanan, G. T. Hitz, E. D. Wachsman and V. Thangadurai, *J. Electrochem. Soc.*, 2015, **162**, A1772-A1777.

7. S. Narayanan, F. Ramezanipour and V. Thangadurai, *Inorg. Chem.*, 2015, **54**, 6968-6977.

8. E. J. Cussen, *J. Mater. Chem.*, 2010, **20**, 5167.

9. E. J. Cussen, *Chem. Commun.*, 2006, 412-413.

10. S. Narayanan, V. Epp, M. Wilkening and V. Thangadurai, *RSC Adv.*, 2012, **2**, 2553.

11. A. Ramzy and V. Thangadurai, *ACS Appl. Mater. Interfaces*, 2010, **2**, 385-390.

12. Y. Li, J.-T. Han, C.-A. Wang, H. Xie and J. B. Goodenough, *J. Mater. Chem.*, 2012, **22**, 15357.

13. V. Thangadurai and W. Weppner, *Adv. Funct. Mater.*, 2005, **15**, 107-112.

14. R. Murugan, V. Thangadurai and W. Weppner, *Angew. Chem. Int. Ed. Engl.*, 2007, **46**, 7778-7781.

15. V. Thangadurai, H. Kaack and W. J. F. Weppner, *J. Am. Ceram. Soc.*, 2003, **86**, 437-440.

16. J. Percival, E. Kendrick, R. I. Smith and P. R. Slater, *Dalton. Trans.*, 2009, 5177-5181.

17. S. Narayanan and V. Thangadurai, *J. Power Sources*, 2011, **196**, 8085-8090.

18. L. van Wullen, T. Echelmeyer, H. W. Meyer and D. Wilmer, *Phys. Chem. Chem. Phys.*, 2007, **9**, 3298-3303.

19. M. Xu, M. S. Park, J. M. Lee, T. Y. Kim, Y. S. Park and E. Ma, *Phys. Rev. B*, 2012, **85**.

20. E. J. Cussen and T. W. S. Yip, *J. Solid State Chem.*, 2007, **180**, 1832-1839.

21. M. P. O'Callaghan and E. J. Cussen, *Chem. Commun.*, 2007, 2048-2050.

22. M. P. O'Callaghan, D. R. Lynham, E. J. Cussen and G. Z. Chen, *Chem. Mater.*, 2006, **18**, 4681-4689.

23. A. Kuhn, V. Epp, G. Schmidt, S. Narayanan, V. Thangadurai and M. Wilkening, *J. Phys. Condens. Mat.*, 2012, **24**, 035901.

24. A. Kuhn, S. Narayanan, L. Spencer, G. Goward, V. Thangadurai and M. Wilkening, *Phys. Rev. B*, 2011, **83**.

25. A. K. Baral, S. Narayanan, F. Ramezanipour and V. Thangadurai, *Phys. Chem. Chem. Phys.*, 2014, **16**, 11356-11365.

26. M. M. Ahmad, *Nanoscale Res. Lett.*, 2015, **10**, 58.

27. M. M. Ahmad, *Ceram. Int.*, 2015, **41**, 6398-6408.

28. C. Deviannapoorani, L. Dhivya, S. Ramakumar and R. Murugan, *J. Power Sources*, 2013, **240**, 18-25.

29. L. Dhivya, N. Janani, B. Palanivel and R. Murugan, *AIP Adv.*, 2013, **3**, 082115.

30. S. Ramakumar, L. Satyanarayana, S. V. Manorama and R. Murugan, *Phys. Chem. Chem. Phys.*, 2013, **15**, 11327-11338.

31. S. Ramakumar, N. Janani and R. Murugan, *Dalton Trans.*, 2015, **44**, 539-552.

32. S. Narayanan, F. Ramezanipour and V. Thangadurai, *J. Phys. Chem. C*, 2012, **116**, 20154-20162.

33. A. M. Phipps and D. N. Hume, *J. Chem. Educ.*, 1968, **45**, 664.

34. A. K. Jonscher, *Nature*, 1977, **267**, 673-679.

35. J. C. Dyre, *J. Appl. Phys.*, 1988, **64**, 2456-2468.

36. K. Funke, *Solid State Ionics*, 1997, **94**, 27-33.

37. J. E. Diosa, R. A. Vargas, I. Albinsson and B. E. Mellander, *Solid State Ionics*, 2006, **177**, 1107-1110.

38. A. Orliukas, A. Dindune, Z. Kanepe, J. Ronis, E. Kazakevicius and A. Kežionis, *Solid State Ionics*, 2003, **157**, 177-181.

39. K. P. Padmasree, R. A. Montalvo-Lozano, S. M. Montemayor and A. F. Fuentes, *J. Alloy. Compd.*, 2011, **509**, 8584-8589.

40. P. B. Macedo, C. T. Moynihan and R. Bose, *Phys. Chem. Glasses*, 1972, **13**, 171-179.

41. S. Choudhary and R. J. Sengwa, *Ind. J. Eng. Mater. Sci.*, 7-15.

42. K. L. Ngai and U. Strom, *Phys. Rev. B*, 1988, **38**, 10350-10356.

43. T. Šalkus, E. Kazakevičius, A. Kežionis, A. Dindune, Z. Kanepe, J. Ronis, J. Emery, A. Boulant, O. Bohnke and A. F. Orliukas, *J. Phys. Condens. Mat.*, 2009, **21**, 185502.

44. A. Saleem and S. A. Suthanthiraraj, *Chem. Sci. Trans.*, 2014, **3**, 847-853.

**Table 1.** The bulk (except bulk + grain-boundary for $Li_{6.5}$-Nb) conductivity of $Li_{5+2x}La_3Nb_{2-x}Y_xO_{12}$ at -22 and 25 °C and the activation energy calculated from Arrhenius plot (Figure 2) at temperature range -50 to 50 °C.

| Sample | $\sigma_{-22\,°C}$ ($Scm^{-1}$) | $\sigma_{25\,°C}$ ($Scm^{-1}$) | $E_a$ (eV) |
|---|---|---|---|
| $Li_{6.5}La_3Nb_{1.25}Y_{0.75}O_{12}$ ($Li_{6.5}$-Nb) | 1.27 x $10^{-5}$ | 2.99 x $10^{-4}$ | 0.42 |
| $Li_6La_3Nb_{1.5}Y_{0.5}O_{12}$ ($Li_6$-Nb) | 4.20 x $10^{-6}$ | 1.87 x $10^{-4}$ | 0.58 |
| $Li_{5.5}La_3Nb_{1.75}Y_{0.25}O_{12}$ ($Li_{5.5}$-Nb) | 1.50 x $10^{-6}$ | 7.18 x $10^{-5}$ | 0.59 |

Table 2. Comparison of ionic conductivity of both Nb and Ta phases of $Li_{5+2x}La_3M_{2-x}Y_xO_{12}$ at specific temperatures.[7, 25, 32]

| | **$Li_{5+2x}La_3Nb_{2-x}Y_xO_{12}$** | | **$Li_{5+2x}La_3Ta_{2-x}Y_xO_{12}$** | |
|---|---|---|---|---|
| | T (ºC) | *σ ($Scm^{-1}$)* | T (ºC) | *σ ($Scm^{-1}$)* |
| **$Li_{6.5}$ - phase** | -21 | 1.60 x $10^{-5}$ | -20 | 9.85 x $10^{-6}$ |
| | -25 | 1.18 x $10^{-5}$ | -25 | 7.29 x $10^{-6}$ |
| **$Li_6$ - phase** | -33 | 1.21 x $10^{-6}$ | -35 | 5.84 x $10^{-8}$ |
| | -40 | 5.48 x $10^{-7}$ | -40 | 3.34 x $10^{-8}$ |
| **$Li_{5.5}$- phase** | -33 | 4.52 x $10^{-7}$ | -35 | 5.94 x $10^{-8}$ |
| | -40 | 2.10 x $10^{-7}$ | -40 | 3.32 x $10^{-8}$ |

**Figure Captions**

**Figure 1.** Typical complex impedance spectra obtained using $Li^+$ ion blocking Au electrodes for $Li_{5.5}La_3Nb_{1.75}Y_{0.25}O_{12}$ ($Li_{5.5}$-Nb), $Li_6La_3Nb_{1.5}Y_{0.5}O_{12}$ ($Li_6$-Nb) and $Li_{6.5}La_3Nb_{1.25}Y_{0.75}O_{12}$ ($Li_{6.5}$-Nb) at about -22 °C. The line spacing through the data point is fitted using an equivalent circuit consisting of $(R_bCPE_b)(CPE_e)$ for $Li_{5.5}$-Nb and $Li_6$-Nb and $(R_b\ CPE_b)\ (R_{gb}\ CPE_{gb})\ (CPE_e)$ for $Li_{6.5}$-Nb.

**Figure 2.** Arrhenius plots of bulk Li ion conductivity of $Li_{5.5}La_3Nb_{1.75}Y_{0.25}O_{12}$ ($Li_{5.5}$-Nb), $Li_6La_3Nb_{1.5}Y_{0.5}O_{12}$ ($Li_6$-Nb), and total (bulk + grain-boundary) $Li^+$ ion conductivity of $Li_{6.5}La_3Nb_{1.25}Y_{0.75}O_{12}$ ($Li_{6.5}$-Nb). The line passing through the data points is fitted line using equation 2.

**Figure 3.** The electrical conductivity of (a) $Li_{5.5}La_3Nb_{1.75}Y_{0.25}O_{12}$ ($Li_{5.5}$-Nb), (b) $Li_6La_3Nb_{1.5}Y_{0.5}O_{12}$ ($Li_6$-Nb) and (c) $Li_{6.5}La_3Nb_{1.25}Y_{0.75}O_{12}$ ($Li_{6.5}$-Nb) as a function of frequency at different temperatures obtained using AC impedance spectroscopy with $Li^+$ ion blocking Au electrodes.

**Figure 4.** Estimated real part of permittivity ($\varepsilon^{/}$) as a function of frequency of (a) $Li_{5.5}La_3Nb_{1.75}Y_{0.25}O_{12}$ ($Li_{5.5}$-Nb), (b) $Li_6La_3Nb_{1.5}Y_{0.5}O_{12}$ ($Li_6$-Nb) and (c) $Li_{6.5}La_3Nb_{1.25}Y_{0.75}O_{12}$ ($Li_{6.5}$-Nb) at different temperatures from AC impedance spectroscopy data collected using $Li^+$ ion blocking Au electrodes.

**Figure 5.** Imaginary part of permittivity ($\varepsilon^{//}$) as a function of frequency of (a) $Li_{5.5}La_3Nb_{1.75}Y_{0.25}O_{12}$ ($Li_{5.5}$-Nb), (b) $Li_6La_3Nb_{1.5}Y_{0.5}O_{12}$ ($Li_6$-Nb) and (c) $Li_{6.5}La_3Nb_{1.25}Y_{0.75}O_{12}$ ($Li_{6.5}$-Nb) at different temperatures.

**Figure 6.** Dielectric tangent loss (δ) as a function of frequency of (a) $Li_{5.5}La_3Nb_{1.75}Y_{0.25}O_{12}$ ($Li_{5.5}$-Nb), (b) $Li_6La_3Nb_{1.5}Y_{0.5}O_{12}$ ($Li_6$-Nb) and (c) $Li_{6.5}La_3Nb_{1.25}Y_{0.75}O_{12}$ ($Li_{6.5}$-Nb) at different temperatures.

**Figure 7.** Comparison of dielectric tangent loss (δ) as a function of frequency of (a) $Li_{5.5}$-, (b) $Li_6$-, and (c) $Li_{6.5}$- phases of both Ta and Nb members of $Li_{5+2x}La_3M_{2-x}Y_xO_{12}$ (M = Nb and Ta[25] at different temperatures.

**Figure 8.** The relative permittivity of $Li_{5.5}$-, $Li_6$-, and $Li_{6.5}$- phases $Li_{5+2x}La_3M_{2-x}Y_xO_{12}$ (M = Nb and Ta) at different temperatures.

**Figure 9.** Electric modulus $M^{//}$ as a function of frequency of (a) $Li_{5.5}La_3Nb_{1.75}Y_{0.25}O_{12}$ ($Li_{5.5}$-Nb), (b) $Li_6La_3Nb_{1.5}Y_{0.5}O_{12}$ ($Li_6$-Nb) and (c) $Li_{6.5}La_3Nb_{1.25}Y_{0.75}O_{12}$ ($Li_{6.5}$-Nb) at different temperatures.

**Figure 10.** Arrhenius plots of relaxation time of (a) $Li_{5.5}La_3Nb_{1.75}Y_{0.25}O_{12}$ ($Li_{5.5}$-Nb), (b) $Li_6La_3Nb_{1.5}Y_{0.5}O_{12}$ ($Li_6$-Nb) and (c) $Li_{6.5}La_3Nb_{1.25}Y_{0.75}O_{12}$ ($Li_{6.5}$-Nb).

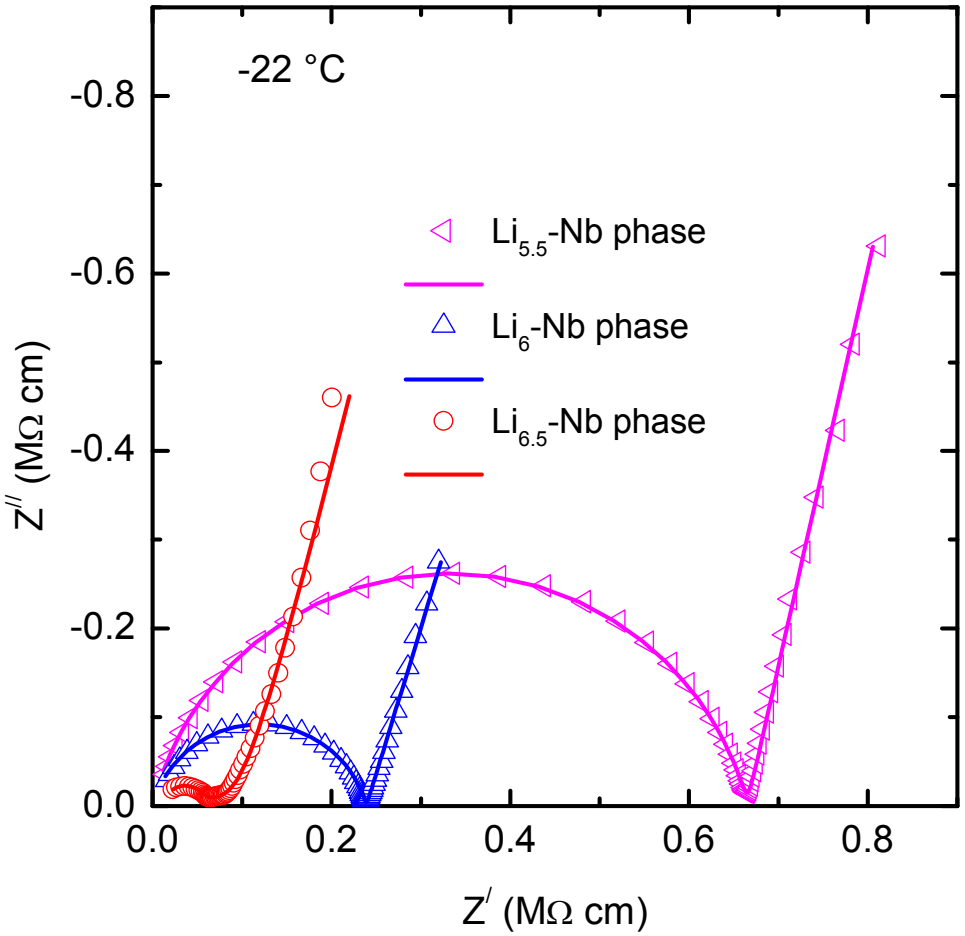
-22 °C
Li5.5-Nb phase
Li6-Nb phase
Li6.5-Nb phase
-0.8
-0.6
-0.4
-0.2
0.0
0.0
0.2
0.4
0.6
0.8
Z// (MΩ cm)
Z/ (MΩ cm)

**Figure 1.**

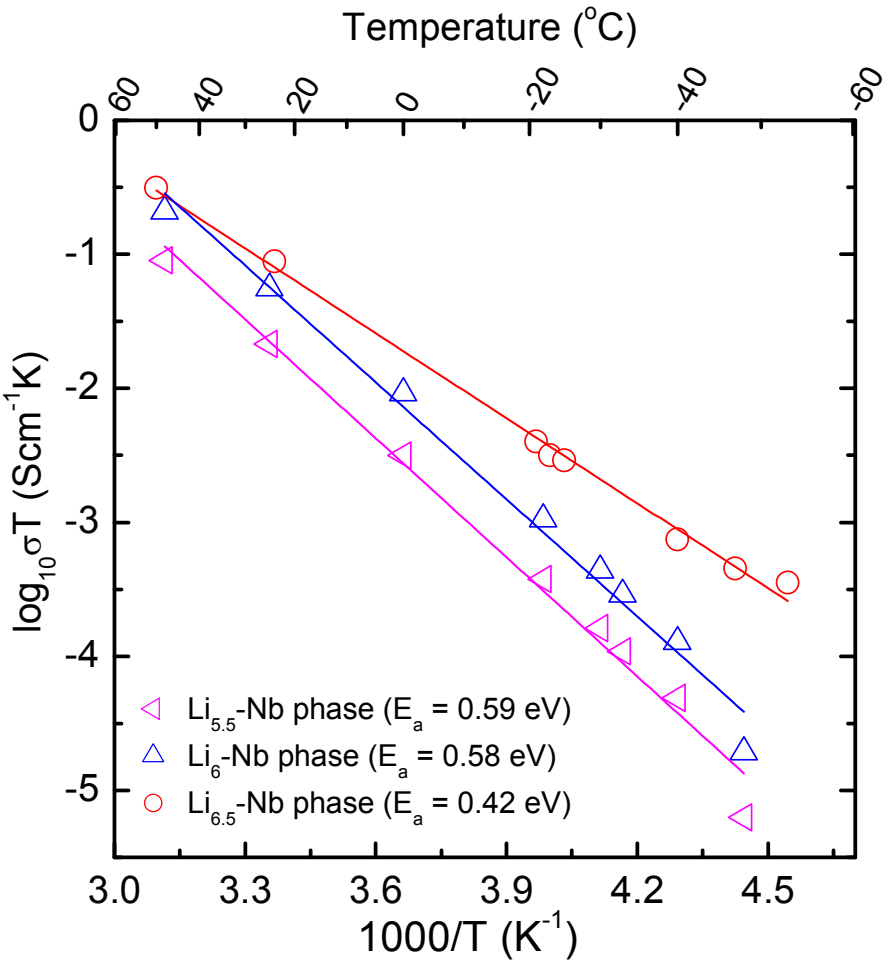
Temperature (°C)
60
40
20
0
-20
-40
-60
0
-1
-2
-3
-4
-5
log10σT (Scm-1K)
Li5.5-Nb phase (Ea = 0.59 eV)
Li6-Nb phase (Ea = 0.58 eV)
Li6.5-Nb phase (Ea = 0.42 eV)
3.0
3.3
3.6
3.9
4.2
4.5
1000/T (K-1)

**Figure 2.**

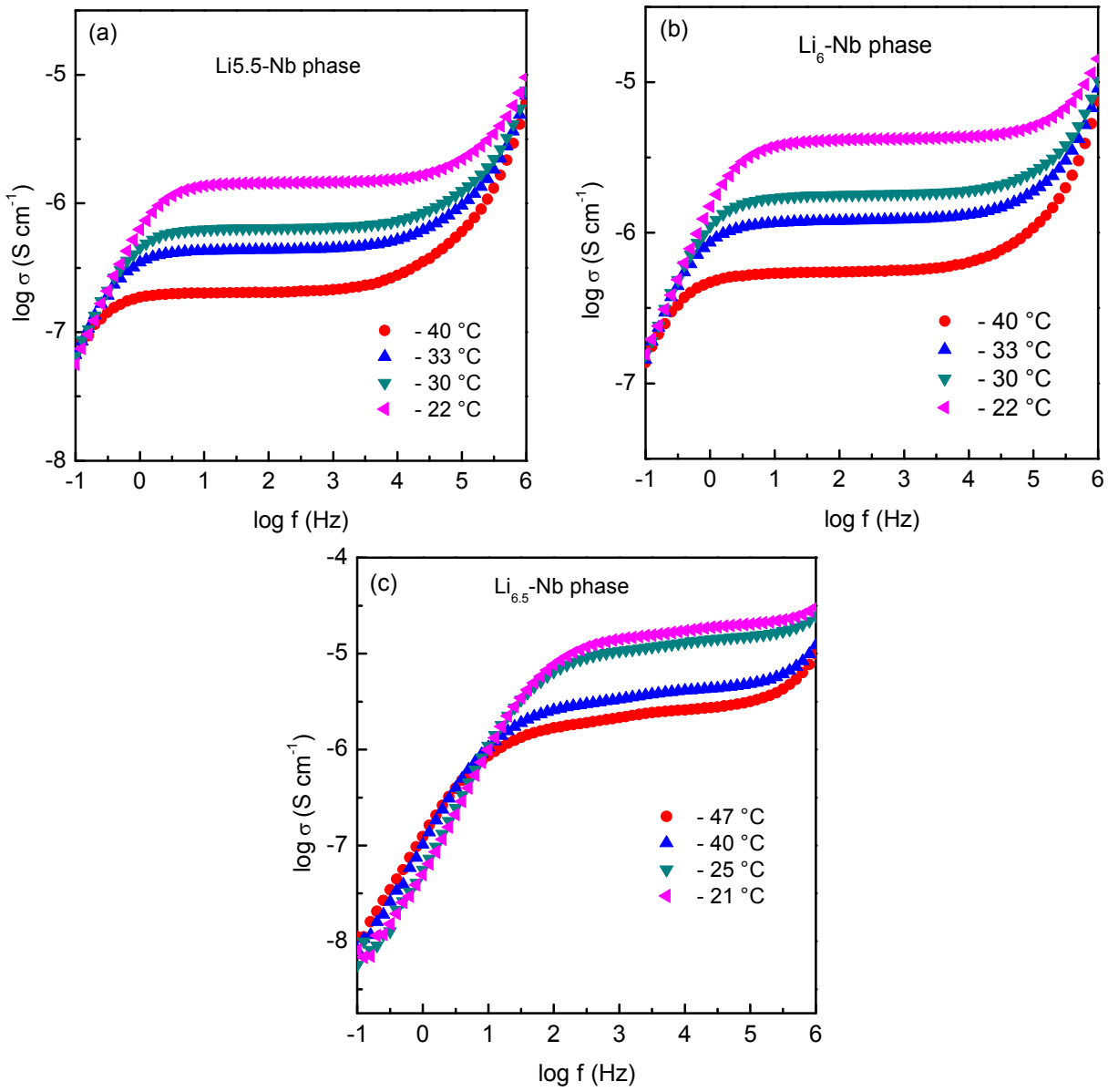
(a)
Li5.5-Nb phase
- 40 °C
- 33 °C
- 30 °C
- 22 °C
log σ (S cm-1)
log f (Hz)
(b)
Li6-Nb phase
- 40 °C
- 33 °C
- 30 °C
- 22 °C
log σ (S cm-1)
log f (Hz)
(c)
Li6.5-Nb phase
- 47 °C
- 40 °C
- 25 °C
- 21 °C
log σ (S cm-1)
log f (Hz)

**Figure 3.**

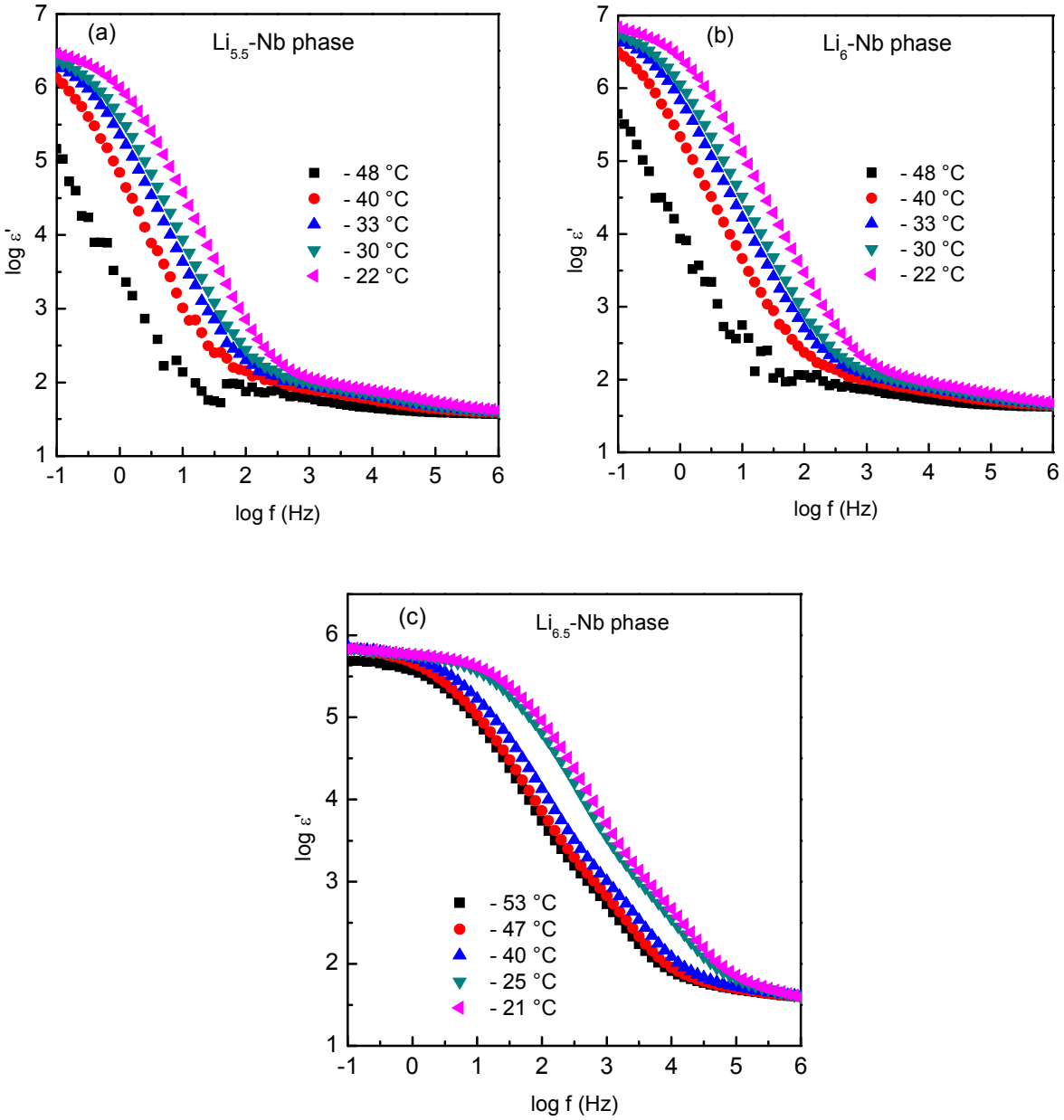
(a)
Li5.5-Nb phase
- 48 °C
- 40 °C
- 33 °C
- 30 °C
- 22 °C
log ε'
log f (Hz)
(b)
Li6-Nb phase
- 48 °C
- 40 °C
- 33 °C
- 30 °C
- 22 °C
log ε'
log f (Hz)
(c)
Li6.5-Nb phase
- 53 °C
- 47 °C
- 40 °C
- 25 °C
- 21 °C
log ε'
log f (Hz)

**Figure 4.**

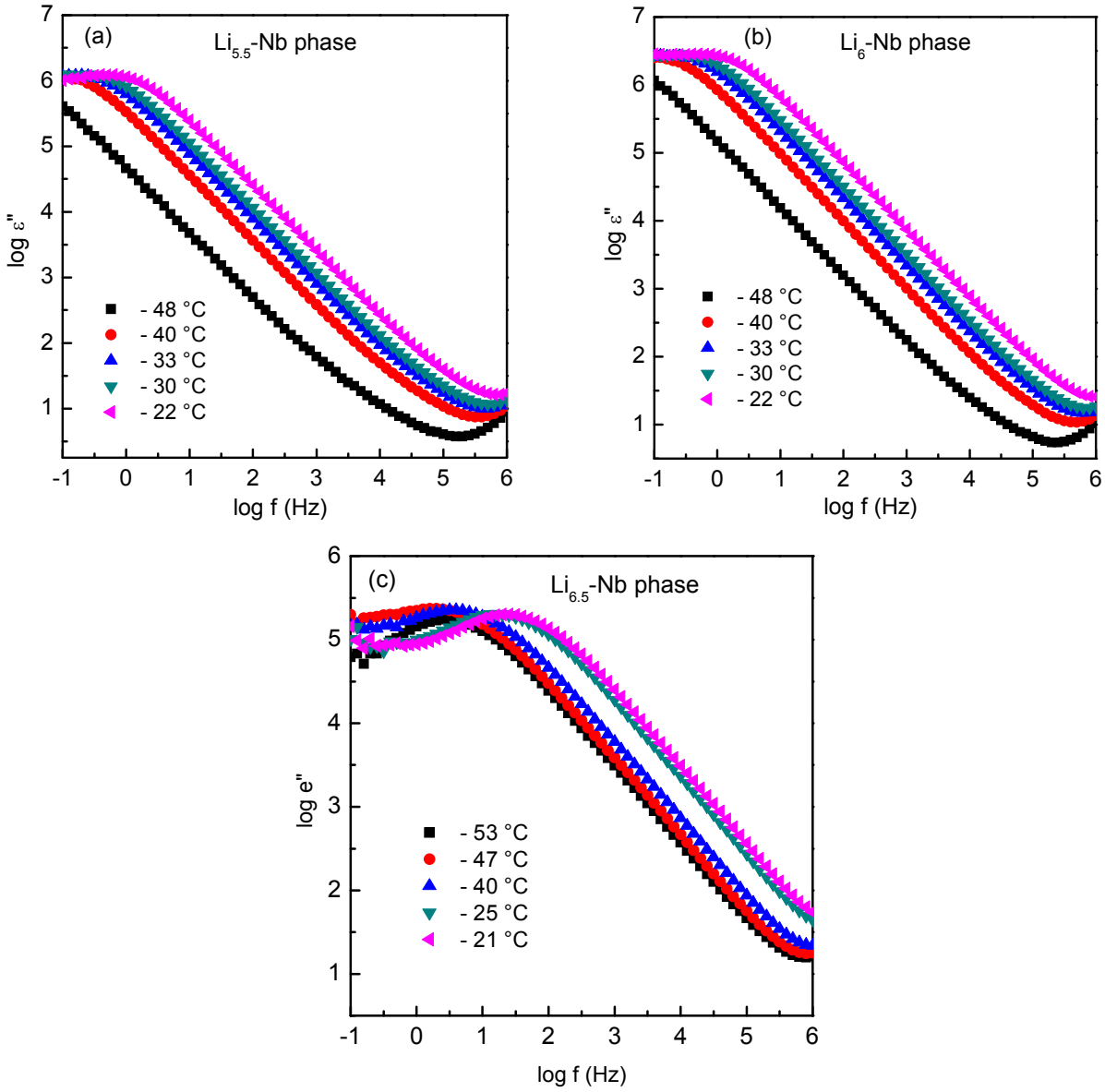
(a)
Li5.5-Nb phase
log ε"
log f (Hz)
- 48 °C
- 40 °C
- 33 °C
- 30 °C
- 22 °C
(b)
Li6-Nb phase
log ε"
log f (Hz)
- 48 °C
- 40 °C
- 33 °C
- 30 °C
- 22 °C
(c)
Li6.5-Nb phase
log e"
log f (Hz)
- 53 °C
- 47 °C
- 40 °C
- 25 °C
- 21 °C

**Figure 5.**

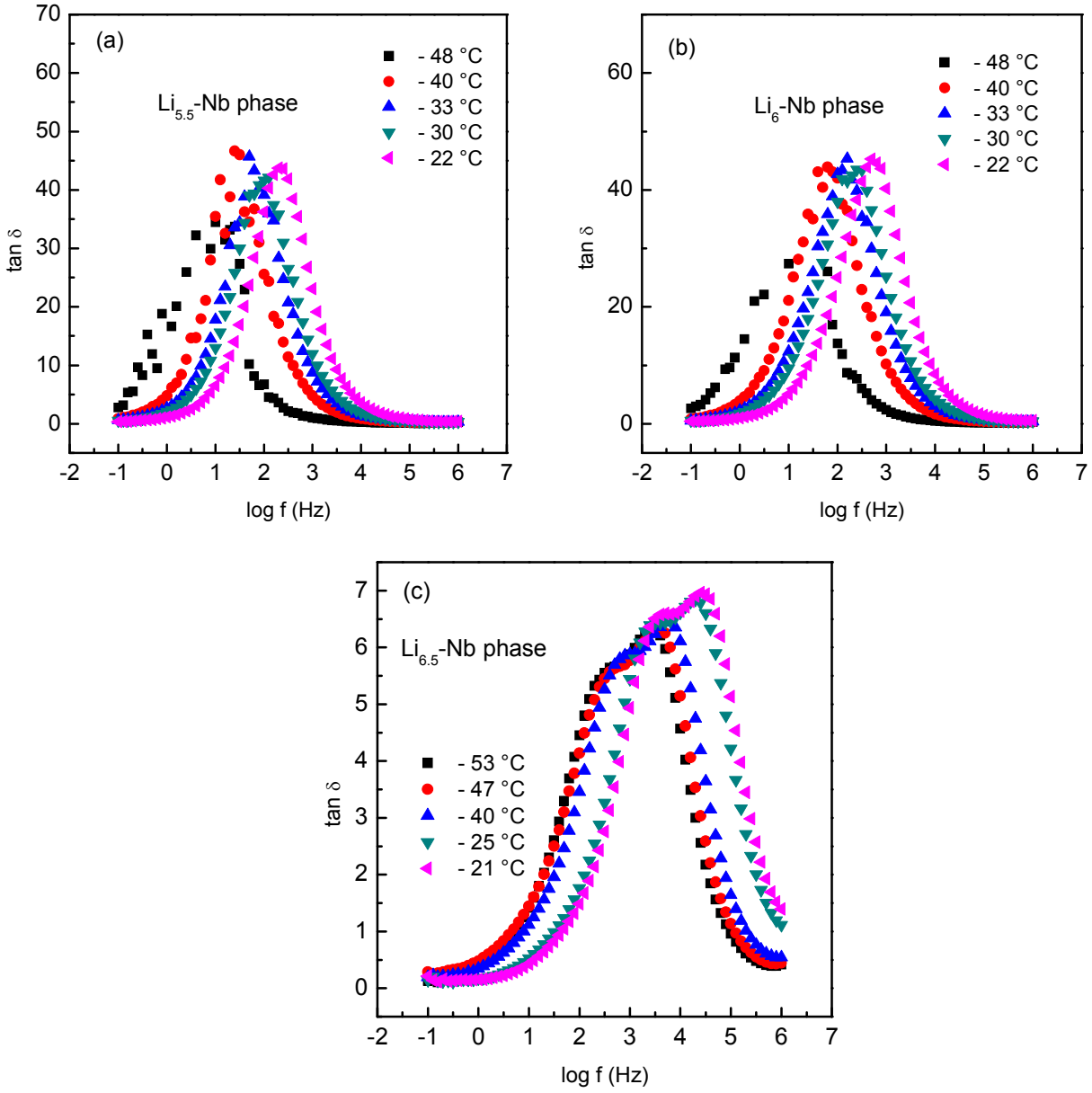
(a)
Li5.5-Nb phase
- 48 °C
- 40 °C
- 33 °C
- 30 °C
- 22 °C
tan δ
log f (Hz)
(b)
Li6-Nb phase
- 48 °C
- 40 °C
- 33 °C
- 30 °C
- 22 °C
tan δ
log f (Hz)
(c)
Li6.5-Nb phase
- 53 °C
- 47 °C
- 40 °C
- 25 °C
- 21 °C
tan δ
log f (Hz)

**Figure 6.**

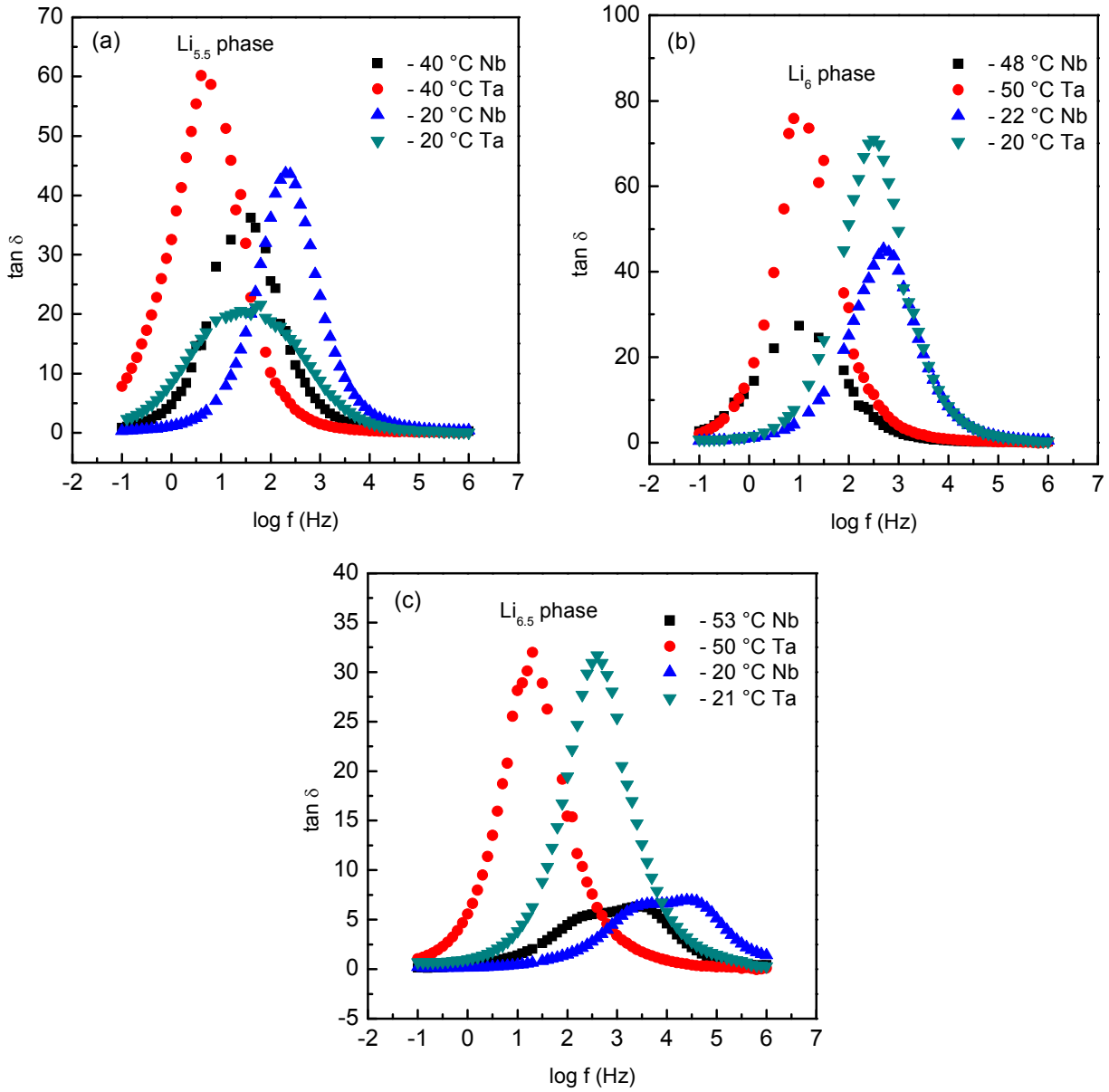
(a)
Li5.5 phase
- 40 °C Nb
- 40 °C Ta
- 20 °C Nb
- 20 °C Ta
tan δ
log f (Hz)
(b)
Li6 phase
- 48 °C Nb
- 50 °C Ta
- 22 °C Nb
- 20 °C Ta
tan δ
log f (Hz)
(c)
Li6.5 phase
- 53 °C Nb
- 50 °C Ta
- 20 °C Nb
- 21 °C Ta
tan δ
log f (Hz)

**Figure 7.**

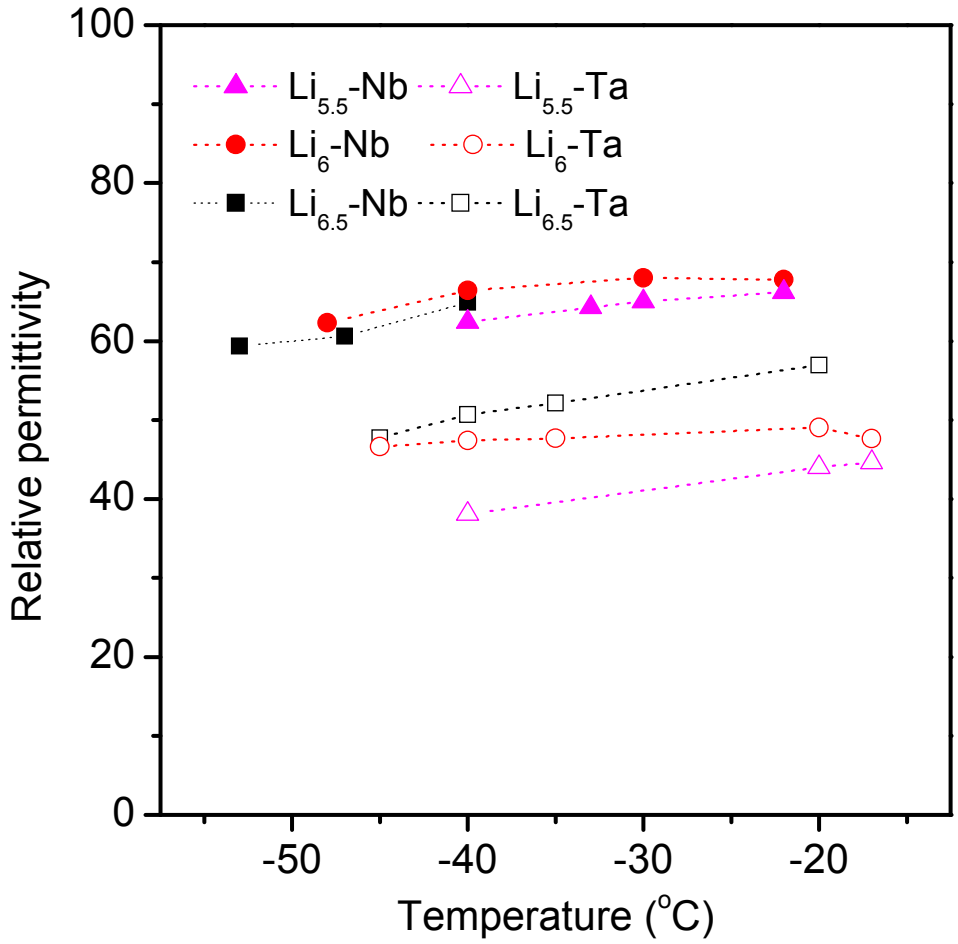
100
80
60
40
20
0
Relative permittivity
-50
-40
-30
-20
Temperature (°C)
Li5.5-Nb
Li5.5-Ta
Li6-Nb
Li6-Ta
Li6.5-Nb
Li6.5-Ta

**Figure 8.**

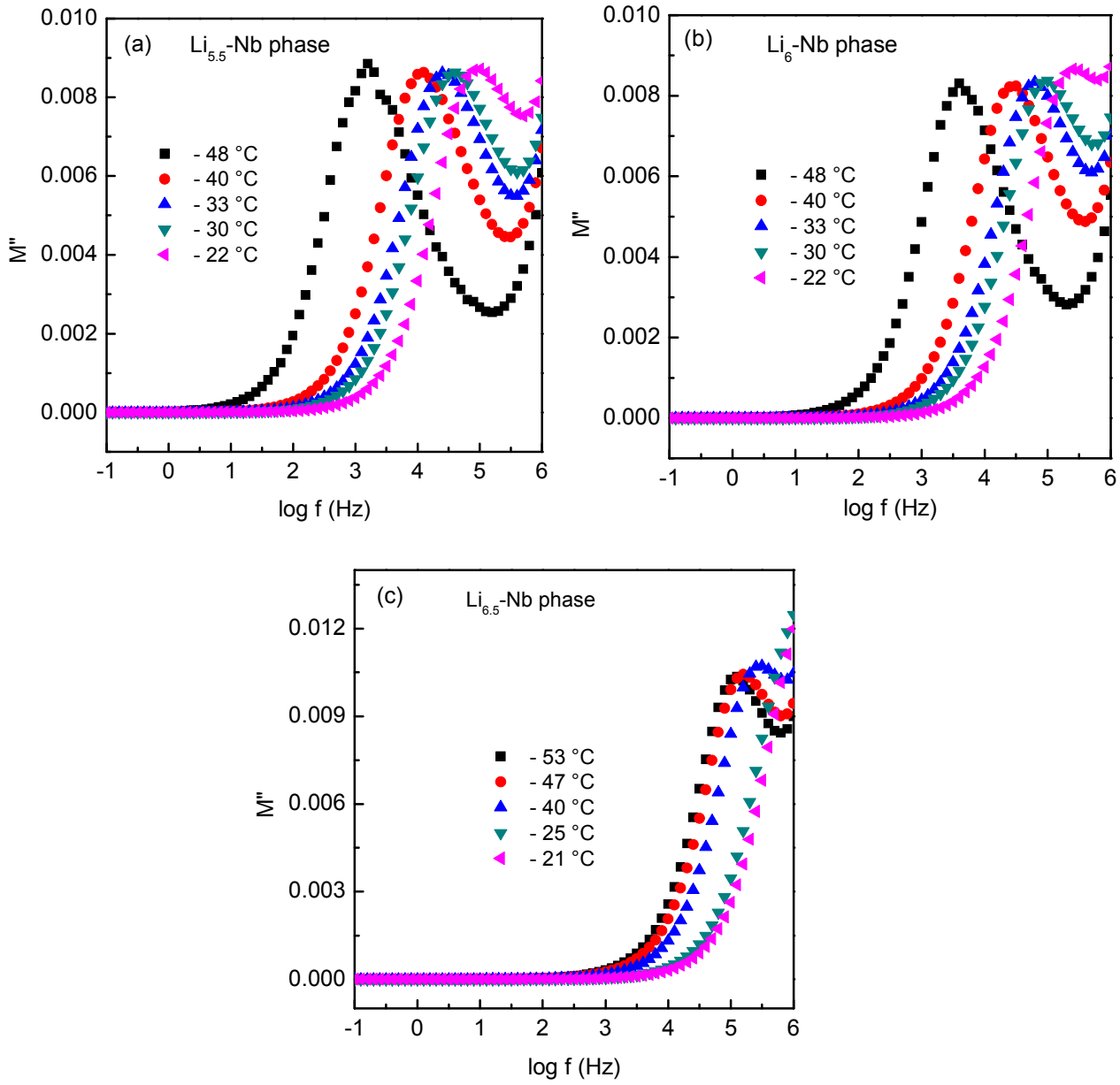
(a) Li5.5-Nb phase
- 48 °C
- 40 °C
- 33 °C
- 30 °C
- 22 °C
M"
log f (Hz)
(b) Li6-Nb phase
- 48 °C
- 40 °C
- 33 °C
- 30 °C
- 22 °C
M"
log f (Hz)
(c) Li6.5-Nb phase
- 53 °C
- 47 °C
- 40 °C
- 25 °C
- 21 °C
M"
log f (Hz)

**Figure 9.**

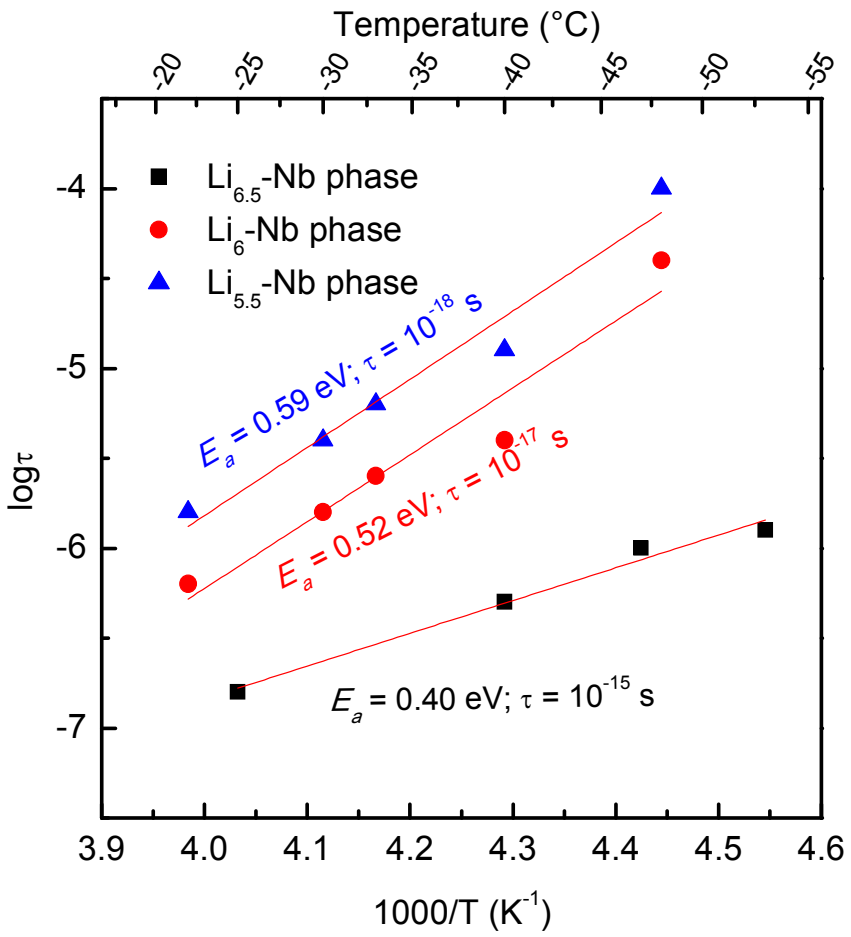
Temperature (°C)
-20
-25
-30
-35
-40
-45
-50
-55
Li6.5-Nb phase
Li6-Nb phase
Li5.5-Nb phase
Ea = 0.59 eV; τ = 10-18 s
Ea = 0.52 eV; τ = 10-17 s
Ea = 0.40 eV; τ = 10-15 s
logτ
-4
-5
-6
-7
3.9
4.0
4.1
4.2
4.3
4.4
4.5
4.6
1000/T (K-1)

**Figure 10.**

**TOC page abstract and figure**

The dielectric characteristics of Li-stuffed $Li_{5+2x}La_3Nb_{2-x}Y_xO_{12}$ garnet-type metal oxides are analyzed in this study using an electrochemical ac impedance spectroscopy to understand the $Li^+$ ion conduction mechanism at low temperatures.